

# Smart Core-Shell Nanostructures for Force, Humidity, and Temperature Multi-Stimuli Responsiveness

Taher Abu Ali, Philipp Schöffner, Maria Beleggratis, Gerburg Schider, Barbara Stadlober, and Anna Maria Coclite\*

A force, humidity, and temperature-responsive electronic skin is presented by combining piezoelectric zinc oxide (ZnO) and poly-N-vinylcaprolactam-co-di(ethylene glycol) divinyl ether hydrogel into core-shell nanostructures using state-of-the-art dry vapor-based techniques. The proposed concept is realized with biocompatible materials in a simplified design that delivers multi-stimuli sensitivity with high spatial resolution, all of which are prerequisites for an efficient electronic skin. While the piezoelectricity of ZnO provides sensitivity to external force, the thermoresponsiveness of the hydrogel core provides sensitivity to surrounding temperature and humidity changes. The hydrogel core exerts mechanical stress onto the ZnO shell, which is translated to a measurable piezoelectric signal. A localized force sensitivity of  $364 \pm 66 \text{ pC N}^{-1}$  is achieved with very low cross talk between  $0.25 \text{ mm}^2$  pixels. Additionally, the sensor's sensitivity to humidity is demonstrated at 25 and 40 °C, i.e., above and below the hydrogel's lower critical solution temperature (LCST) of 34 °C. The largest response to temperature is obtained at high humidity and below the hydrogel's LCST. The sensor response to force, humidity, and temperature is significantly faster than the system's intrinsic or excitation-induced time scale. Finally, the sensor response to touch and breath demonstrates its applicability as e-skin in real-life environment.

stimuli and transmits the information to the brain.<sup>[1]</sup> In the last decade, a substantial understanding of how this complex system behaves has been gained.<sup>[2–4]</sup> Nevertheless, its replication to form artificial skins is still a relatively new field with massive potential. Relying on advancements in functional materials, structural design, and state-of-art production/deposition techniques, a wide variety of single/multi-stimuli responsive sensory systems, suitable for electronic skin (e-skin) applications, have been reported.<sup>[5–8]</sup> An efficient e-skin design requires a combination of functional materials with suitable mechanical and electrical properties,<sup>[9]</sup> in addition to the micro/nanoscale control of the layer's thickness and dimensions, which is optimized by the choice of suitable fabrication techniques.

For pressure and force detection, the most common methods exploit piezoelectric, piezoresistive, or capacitive sensing.<sup>[10–13]</sup> Bao's group investigated an e-skin design based on flexible pressure-sensitive organic thin-film transistors deploying a force-sensitive gate dielectric capacitance. The sensor has

a maximum sensitivity of  $8.4 \text{ kPa}^{-1}$  and a fast response time of 10 ms. This was realized with a combination of microstructured polydimethylsiloxane (PDMS) gate dielectric and a high-mobility semiconducting polymer in a transistor design. The sensor relies on capacitance change due to mechanical excitations.<sup>[14]</sup> Another pressure-sensitive e-skin design, investigated by Bao's group, is realized by a composite piezoresistive material consisting of an organic polymer and nickel nanostructured microparticles.<sup>[15]</sup> Park and Jang investigated hybrid piezoelectric/piezoresistive pressure sensors based on a nanohybrid material from graphene with free-standing nanofibers of PEDOT/P(VDF-HFP). Their e-skin device impresses with a gauge factor as high as 320 under tensile strain thus showing high sensitivity to pressure with a low limit of detection of 0.5 Pa only.<sup>[16]</sup>

Humidity sensors for e-skin applications have also been investigated.<sup>[17,18]</sup> Guo et al. demonstrated that a tungsten sulfide ( $\text{WS}_2$ ) film combined with graphene electrodes and PDMS substrate exhibits a high humidity response (up to 90% relative humidity or RH) due to the change in the  $\text{WS}_2$  conductivity.<sup>[19]</sup> Similarly, e-skin sensitivity to changes in surrounding temperature is desired and has been investigated.<sup>[20–22]</sup> Chen et al.

## 1. Introduction

The human skin is composed of a complex and specialized sensory system, which detects surrounding environmental

T. Abu Ali, A. M. Coclite  
Institute of Solid State Physics  
Graz University of Technology  
Petersgasse 16, Graz 8010, Austria  
E-mail: anna.coclite@tugraz.at

T. Abu Ali, P. Schöffner, M. Beleggratis, G. Schider, B. Stadlober  
Institute for Surface Technologies and Photonics  
Joanneum Research  
Franz-Pichler-Straße 30, Weiz 8160, Austria

 The ORCID identification number(s) for the author(s) of this article can be found under <https://doi.org/10.1002/admt.202200246>.

© 2022 The Authors. Advanced Materials Technologies published by Wiley-VCH GmbH. This is an open access article under the terms of the Creative Commons Attribution-NonCommercial License, which permits use, distribution and reproduction in any medium, provided the original work is properly cited and is not used for commercial purposes.

DOI: 10.1002/admt.202200246

presented a flexible temperature sensor for e-skin application based on a semipermeable polyurethane active layer, where its resistivity changes noticeably with the surrounding temperature.<sup>[23]</sup>

The above-discussed concepts rely on sensors for a single physical stimulus. However, multi-stimuli responsiveness is a prerequisite for an efficient e-skin. Several examples of multi-stimuli responsive e-skins are present in the literature.<sup>[24–29]</sup> Ho et al. developed a transparent and stretchable all-graphene multifunctional e-skin sensor matrix sensitive to humidity, temperature, and pressure.<sup>[30]</sup> Another concept of multi-stimuli responsive sensors is presented by Han et al., in which an organic aerogel with mixed ion–electron conductivity is developed to be sensitive to pressure, temperature, and humidity with minimal cross-talk.<sup>[31]</sup> However, of the above-mentioned sensor solutions, none can demonstrate multi-stimuli responsiveness and location-specific stimuli-response all at once and they also lack a simplified architecture as well as biocompatible materials.

In this publication, we demonstrate a flexible skin-like sensor that is responsive to multiple stimuli (force, humidity, and temperature, abbreviated as F-H-T) and, since constructed as an array of vertical nanorod pixels, reacts in a location-specific manner to said stimuli. The active layer is made of an array of core-shell nanorods consisting of a Poly-N-vinylcaprolactam-co-di(ethylene glycol) divinyl ether (p(NVCL-co-DEGDVE)) hydrogel core and a zinc oxide (ZnO) piezoelectric shell. The choice of p(NVCL) hydrogel is due to its thermoresponsive nature. p(NVCL), which is non-toxic and biocompatible,<sup>[32]</sup> possesses hydrophilic functional groups (caprolactam ring) that bond with water molecules. This bonding mechanism is dependent on a specific temperature defined as the lower critical solution temperature (LCST): the hydrogel undergoes a phase transition from a swollen hydrated state below to a shrunken dehydrated state above the LCST, resulting in desired sensitivity to temperature and humidity. In a previous contribution, we showed that the LCST can be tailored by copolymerization of the NVCL with DEGDVE. This, beyond being a cross-linker, adds hydrophobic functional groups to the polymer chains reducing the LCST of p(NVCL).<sup>[33]</sup>

In our design, temperature and humidity changes in the surrounding environment are sensed by the p(NVCL-co-DEGDVE) core, which swells as a result (Figure 1a). The hydrogel swelling mechanically strains the ZnO shell and a measurable current/charge is in turn generated due to its piezoelectric nature.<sup>[34]</sup> Apart from this indirectly induced mechanical stress, an applied force can be directly sensed by the ZnO shell. The choice of ZnO for the shell is based on several advantages related to this material. First, it exhibits both semiconducting and piezoelectric properties that can be used to transform mechanical stresses into electric current for electromechanically coupled sensors and transducers.<sup>[35]</sup> Second, ZnO is relatively biosafe and biocompatible, and it can be used for biomedical applications with little toxicity.

Arrays of core-shell structures, like the one schematized in Figure 1a, can be obtained by subsequent deposition in porous templates. The template-deposition of polymers or of inorganic materials requires the coating of high-aspect-ratio nanopores with high conformality. Liquid phase-based or line-of-sight

deposition methods (sputtering, plasma-assisted chemical vapor deposition, evaporation) may not uniformly fill the pores, resulting in low-quality nanorods. Therefore, we used initiated chemical vapor deposition (iCVD) for the hydrogel core and plasma-enhanced atomic layer deposition (PEALD) for the ZnO shell. Both these techniques are driven by surface-limited reactions, which ensure highly conformal coating and/or filling of the template pores. We previously demonstrated that the piezoelectric properties of ZnO deposited by PEALD depend on the deposition temperature, where a film of ZnO as thin as 50 nm deposited on a glass/ITO substrate at 25 °C exhibits an apparent  $d_{33}$  coefficient of 3 pC N<sup>-1</sup>, which increases to 20 pC N<sup>-1</sup> when deposited at 225 °C.<sup>[36]</sup>

Skin-like sensors usually consist of an array of touch-sensitive sites, called tactile pixels or taxels, which may be capable of measuring more than one property.<sup>[15]</sup> In nature, tactile recognition, that is, the detection of object features, such as surface texture and fine form discrimination, is carried out by a large number of corpuscles and free nerve endings sensitive to mechanical stimuli (mechanoreceptors). Psychophysical studies have shown that the limiting spatial resolution of human fingertips is of the order of 1 mm.<sup>[1]</sup> Skin normally experiences multi-axial forces and undergoes a range of angular and linear motions at different body locations. This heterogeneity in movements and strains of skin suggests the need for location-specific optimization of sensors in artificial skins and prosthetics.<sup>[37]</sup> Kim et al.<sup>[26]</sup> have achieved such location-specificity in a prosthetic skin equipped with a series of different sensors for strain, pressure, and temperature in a multi-layered device. Different sensors for each stimulus were used (e.g., a sensor for strain, another for temperature, another for pressure) and dislocated into the matrix with a quite laborious architecture. To achieve high resolution and multi-sensitivity at the same time we used a completely different device architecture, based on vertical sensing nanorods with a lateral dimension of only 500 nm, instead of horizontal layers. Each pixel of our device contains thousands of sensing nanorods and the signal is read out electronically at every individual pixel.

## 2. Results and Discussion

The core-shell nanorods are embedded in a polyurethane acrylate (PUA) polymeric template that is nanopatterned by UV-nanoimprint lithography (UV-NIL). The nanostructured layer is then sandwiched between two electrodes. The detailed fabrication steps of the core-shell nanorod array are shown in Figure 1b (thickness of layers not shown to scale). Starting with a polyethylene terephthalate (PET) substrate, a bottom electrode (BE) of chromium/silver (Cr/Ag) with thickness of 2.5/50 nm is first deposited by thermal evaporation through a shadow mask. Then, UV-NIL is utilized to imprint nanoholes into a layer of PUA deposited on top with a stamp (Figure S1a, Supporting Information) featuring nanorods, as shown in Figure S1b, Supporting Information. During the imprint process, a force  $F = 30$  N is applied onto the stamp for 30 min, which reduces the thickness of the PUA layer to  $\approx 6$   $\mu$ m (Figure S1c, Supporting Information). The resulting nanoholes (diameter  $d = 500$  nm and height  $H = 500$  nm)

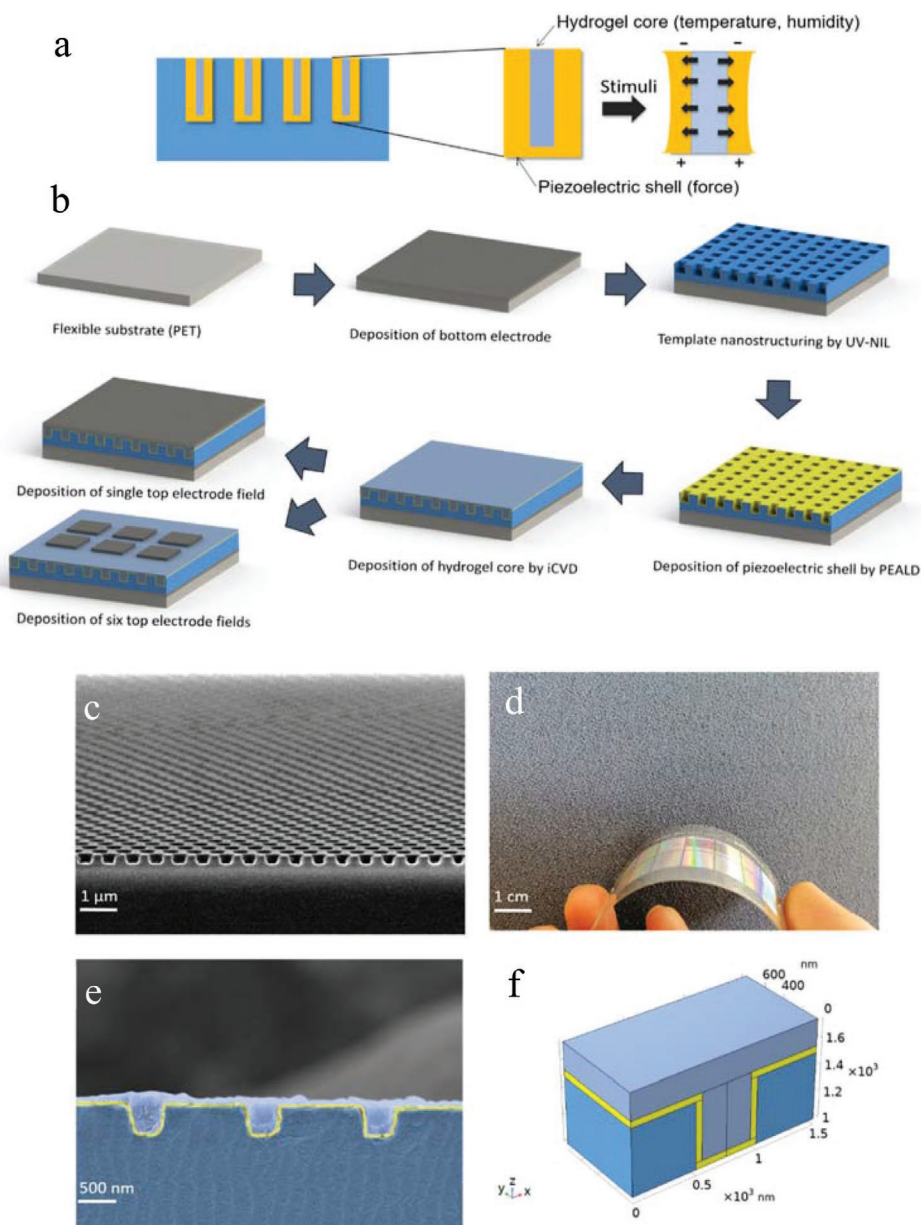


**Figure 1.** a) Cross-sectional view of the core-shell nanorod sensing concept, where force is directly sensed by a ZnO piezoelectric shell. The hydrogel core, which swells, senses humidity and temperature changes, and a resultant stress is applied onto the ZnO piezoelectric shell. b) F-H-T responsive sensor fabrication routine (dimensions are not shown to scale). Starting with a PET substrate, a BE is deposited using e-beam evaporation. A PUA template layer is then applied and nanostructured using UV-NIL. The ZnO piezoelectric shell is deposited using PEALD. Next, the hydrogel core consisting of p(NVCL-co-DEGDVE) is deposited using iCVD and finally, two TE designs are deposited with e-beam evaporation (indicated as single electrode field and six electrode fields). c) Scanning electron microscopy (SEM) image of a patterned PUA template prior to filling with core-shell structures. d) Photograph of the complete sensor design with a 1 cm<sup>2</sup> TE active area under bending. e) Colorized SEM image featuring three core-shell nanorod structures: a conformal ZnO shell (yellow) deposited on the nanopatterned PUA (dark blue) and the hydrogel core (navy blue) completely filling the nanoholes. f) Corresponding geometry model used for finite element method (FEM) simulations.

prior to deposition of the core-shell layers are shown in Figure 1c. Subsequently, deposition of the ZnO shell with a thickness of 50 nm is carried out at 35 °C using PEALD, followed by deposition of the p(NVCL-co-DEGDVE) core with a thickness of 200 nm via iCVD. As a last fabrication step, two designs of an Ag top electrode (TE) with a thickness of 50 nm are deposited by evaporation through respective shadow

masks. The first design is composed of a single TE field with an active area of 1 cm<sup>2</sup> (Figure 1d). The second design is composed of six TE fields, each with an active area of 0.25 mm<sup>2</sup> and spaced 5 mm apart. The fabrication of the sensor consists exclusively of process steps that can be carried out sequentially in a pilot line, such as vacuum evaporation for the electrodes, nanoimprint lithography, and chemical vapor deposition (for

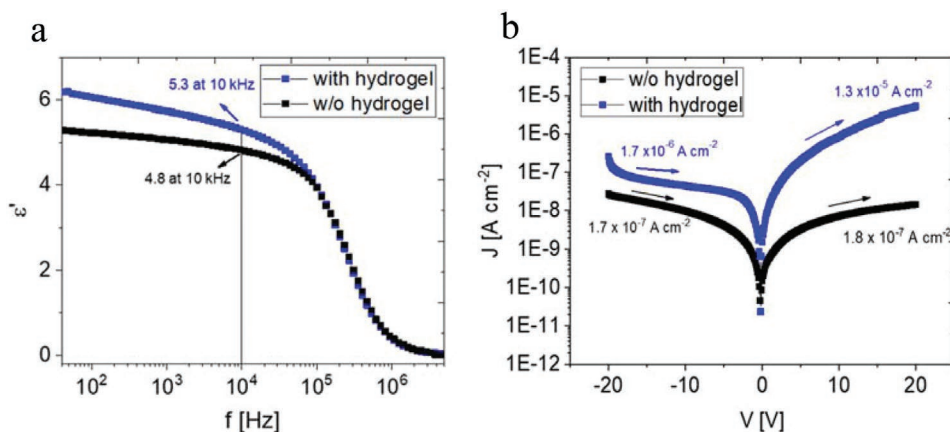


**Figure 2.** a) Real part of dielectric constant  $\epsilon'$  measured as a function of frequency  $f$  in the range of 42 Hz - 5 MHz for a sensor with and without a hydrogel core. b) Current-Voltage (I-V) characterization performed at  $V = \pm 20$  V for a sensor with and without a hydrogel core.

the hydrogel core and the piezoelectric shell). The areal density of the nanorods and their individual diameter, as well as aspect ratio, were optimized by means of simulation to result in a maximized response per unit area within the constraints given by the fabrication method. This resulted in an areal density of  $10^8$  nanorods per  $1 \text{ cm}^2$  of electrode area while the diameter and aspect ratio were large enough to form sufficiently thick ZnO and hydrogel layers giving a high individual response. COMSOL simulations have shown that the optimal pitch is 1000 nm, with nanorods of 500 nm in diameter spaced over 500 nm.

Figure 1c corresponds to the cross-sectional SEM image of a patterned PUA template prior to filling, whereby Figure 1e is an SEM close-up of three nanoholes after filling with a thin ZnO layer (50 nm) and hydrogel (200 nm). It can be observed that the techniques used to deposit the core-shell nanorods deliver the desired uniform profiles: conformal ZnO deposition by PEALD and complete filling of nanoholes with the iCVD-deposited hydrogel core. The iCVD deposition conditions were optimized to achieve a fractional saturation pressure for the monomer and cross-linker at 0.15 and 0.04, respectively, which is recommended for conformal layer coating.<sup>[38]</sup> During cross-sectional cuts of samples for SEM imaging, slight delamination was observed within some nanoholes due to the difference in Young's modulus  $E$  of the PUA template and ZnO.<sup>[39-43]</sup>

The working principle of the as-fabricated device is based on the deformation of the piezoelectric shell induced by the swelling of the hydrogel. Previous work published by our group extensively characterized the swelling behavior of p(NVCL-co-DEGDVE) films on Si (100) substrate, deposited using the same iCVD reactor/conditions used in this work.<sup>[33]</sup> It is indicated that films with 10% nominal cross-linking experienced the highest swelling response in water (represented by the ratio of thickness upon swelling to dry thickness,  $d/d_{\text{dry}}$ ) but delaminated from the substrate during prolonged water-exposure and therefore were unstable.<sup>[33]</sup> Stable films were obtained with 20% nominal cross-linking. In the present work, p(NVCL-co-DEGDVE) films with 25% nominal cross-linking have been deposited for improved stability. The cross-linker fraction influences the LCST of the hydrogel (increasing cross-linker fraction decreases the LCST). For p(NVCL-co-DEGDVE) with a

25% nominal cross-linker fraction, the LCST is measured at  $34 \pm 2 \text{ }^\circ\text{C}$ .<sup>[33]</sup>

The swelling behavior of the hydrogel core is of high importance to simulate the sensor performance with respect to humidity and temperature. Within the finite element method (FEM) simulation, the symmetrical geometry allows to model one half of a nanorod. Figure 1f shows the geometry used for the simulations: a section of the patterned PUA template (colored in blue), bare, with 50 nm of conformal ZnO layer (colored in yellow) and with complete filling of the nanohole by the hydrogel core (colored in navy blue). The hydrogel swelling behavior is modeled following Equation (1):

$$\varepsilon = \beta \times C_{\text{mo}} \quad (1)$$

Where,  $\varepsilon$  is the hygroscopic strain exerted by the hydrogel core on the ZnO shell.  $\beta$  is the hydrogel swelling coefficient ( $\text{m}^3 \text{ kg}^{-1}$ ) and  $C_{\text{mo}}$  is the moisture concentration in air ( $\text{kg m}^{-3}$ ; equivalent to RH %). Table S1, Supporting Information, shows  $\beta$  and  $C_{\text{mo}}$  values calculated for p(NVCL-co-DEGDVE) 25% nominally cross-linked grown on ZnO (50 nm) on a Si substrate.  $\beta$  is calculated at 10, 25, 35, 40, and 50  $^\circ\text{C}$  (below and above LCST) at different RH% ( $C_{\text{mo}}$ ). In addition to simulating the response to humidity and temperature, the simulated sensor response to force is performed by applying a boundary load condition, where the input force is given per unit area ( $\text{N m}^{-2}$ ).

Characterization of the sensor dielectric properties, as well as I-V response, is performed in order to assess the current flow from bottom to TE across the template, which acts as a dielectric layer. **Figure 2a** shows the real part of the dielectric constant  $\epsilon'$ , which is measured in the frequency range  $f = 42$  Hz up to 5 MHz for a sensor with a hydrogel core in comparison to a reference sensor without a hydrogel core. The measurements were performed on a sensor with an active TE area of  $1 \text{ cm}^2$ . At 42 Hz, the dielectric constant amounts to 6.3 for the sensor with a hydrogel core and 5.3 for the sensor without the hydrogel core.  $\epsilon'$  drops to 5.3 and 4.7 at  $f = 10$  kHz, respectively. The sharp drop in  $\epsilon'$  between 10 kHz and 1 MHz is related to dipolar relaxation, which typically occurs between 1 Hz and 100 MHz for polymers.<sup>[44]</sup> The dielectric properties of the hydrogel are influenced

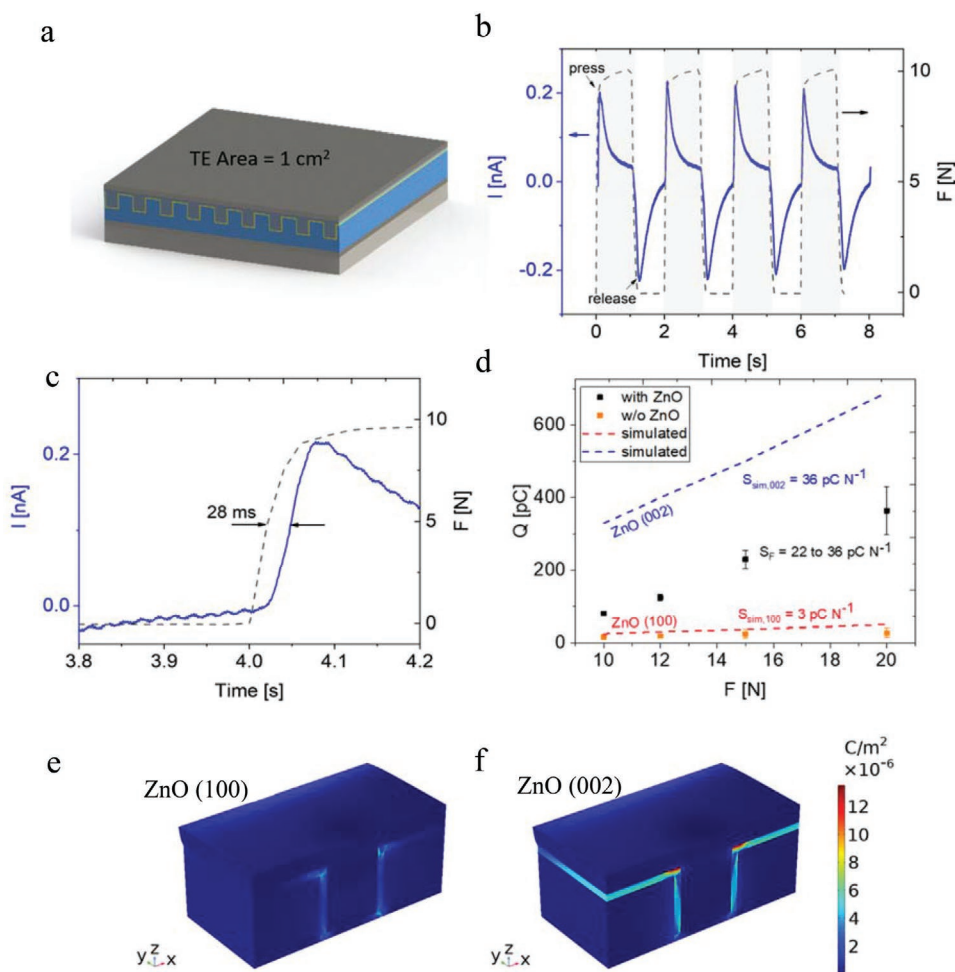


**Figure 3.** a) Schematics of a sensor with a TE active area of  $1 \text{ cm}^2$  (dimensions are not shown to scale). b) Current  $I$  response over time  $t$  to a 10 N step force stimulus. c) Zoom-in of Figure 3b showing the sensor response time to 10 N step force stimulus. d) Charge  $Q$  (integrated current signal) as a function of excitation force (10, 12, 15, and 20 N) for a sensor with ZnO, a reference sensor without ZnO as well as the simulated response using FEM simulations. The variation in the charge response for a given force level (error bars) is calculated from three measurements each performed on two sensors (sample size,  $n = 6$ ). The sensor sensitivity to force,  $S_F$ , is also reported in the Figure 3D polarization distribution spatial maps (cf. color bar) obtained from FEM simulation on piezoelectric ZnO with (e) (100) preferential orientation and (f) with (002) preferential orientation.

by the moisture content inside its polymeric mesh, where the dielectric constant of water is  $\approx 80$ .<sup>[45]</sup> However, in its dry state, a thermoresponsive hydrogel typically shows  $\epsilon'$  values of 3 to 4.<sup>[46]</sup> Moreover, due to the measurements being performed in ambient humidity conditions (40% RH) and the much thinner hydrogel core layer in comparison to the PUA template layer ( $200 \text{ nm} \ll 6 \text{ }\mu\text{m}$ ), the sensor overall  $\epsilon'$  is mainly dependent on the thickness and dielectric properties of the PUA layer (see supporting note 1 for calculation of theoretical dielectric constant).  $I$ - $V$  characterization curves were measured for both sensors (with and without the hydrogel core) in the voltage range  $V = \pm 20 \text{ V}$  (Figure 2b). For the sensor with a hydrogel core, the measured current density  $J$  is  $1.7 \times 10^{-6} \text{ A cm}^{-2}$  at  $-20 \text{ V}$  and  $1.3 \times 10^{-5} \text{ A cm}^{-2}$  at  $+20 \text{ V}$ . For the sensor without a hydrogel core (reference),  $J = 1.7 \times 10^{-7} \text{ A cm}^{-2}$  and  $1.8 \times 10^{-7} \text{ A cm}^{-2}$  at  $-20 \text{ V}$  and  $+20 \text{ V}$ , respectively. The results indicate that the hydrogel core increases the leakage current of the sensor. The current density asymmetry is related to charging effects, which are enhanced with the presence of a sensor with a hydrogel core.

## 2.1. Full-Area Force Response

Figure 3a–d shows the sensor scheme (single TE with an active area of  $1 \text{ cm}^2$ ) and response to external force stimuli, where different force intensities of  $F = 10, 12, 15,$  and  $20 \text{ N}$  were applied using a piezoelectric test setup, as schematized in Figure S2a, Supporting Information. Figure 3b shows the generated current as a function of time for a step excitation force signal of 10 N for 4 cycles, with a maximum current  $I$  of  $0.21 \pm 0.02 \text{ nA}$  measured upon pressing with a rounded pneumatic stamp (diameter  $d = 5 \text{ mm}$ ). A zoomed-in graph shows a sensor response time of  $\approx 28 \text{ ms}$  (Figure 3c). The charge  $Q$  is calculated from integrating  $I$  over time  $t$  and is plotted as a function of the force (Figure 3d).

As observed from Figure 3c, upon a force excitation of  $F = 10 \text{ N}$ , a charge response of  $81.0 \pm 1.7 \text{ pC}$  is measured, increasing to  $364 \pm 66 \text{ pC}$  at  $F = 20 \text{ N}$ . The charge response corresponds in good approximation linearly to the force, with an apparent offset. This offset can be related to a high deformation/compression of the hydrogel layer at low forces, thus lowering the

stress exerted onto the ZnO layer. The sensor sensitivity to force excitations,  $S_F$ , is calculated following Equation (2).

$$S_F = \Delta Q / \Delta F \quad (2)$$

It amounts to 22–36 pC N<sup>-1</sup>. The upper sensitivity limit of the experimental data matches the sensitivity  $S_{\text{sim},002} = 36 \text{ pC N}^{-1}$  calculated from the FEM model, where ZnO (002) is considered. A reference sensor response (without ZnO shell and hydrogel core) was measured at  $F = 10, 12, 15,$  and  $20 \text{ N}$  with a maximum  $Q = 28 \pm 12 \text{ pC}$ . Given that the response is significantly lower than what is measured with a fully fabricated sensor containing the core-shell nanostructures, we can conclude that the sensor response to force is due to piezoelectric ZnO. The FEM model delivered different charge values compared to the ones measured experimentally. Such difference is attributed to two factors: first, ZnO deposited at 35 °C crystallizes mainly into (100) crystallographic orientation (piezoelectric polar axis is parallel to substrate surface),<sup>[36,47,48]</sup> but also (002) crystallographic orientation (piezoelectric polar axis perpendicular to substrate surface). The presence of (002) orientated crystallites in ZnO enhances the piezoelectric response to force excitation parallel to the z-axis.<sup>[36,49–51]</sup> In the FEM model, ZnO is single crystalline, therefore the piezoelectric axis is oriented either completely along the (100) direction, or completely along the (002) one. As shown in Figure 3d, the piezoelectric charge obtained from the simulation with a (002) oriented ZnO single crystal is higher than the piezoelectric charge obtained from the simulation with (100) orientation.

The experimental results lie in between these two extreme cases, which is expectable, considering that the ZnO deposited by PEALD at 35 °C has both (100) and (002) oriented crystals.

Another contribution affecting the force response comes from substrate bending, which has to be considered for the flexible PET substrates used. Bending of the substrate generates charges through the transverse piezoelectric effect (attributed to the  $d_{31}$  coefficient of piezoelectric ZnO) in addition to the longitudinal piezoelectric effect (attributed to the  $d_{33}$  coefficient of piezoelectric ZnO), which increases the measured piezoelectric charge.<sup>[52,53]</sup> In the FEM simulation of a single nanorod the substrate is not considered and the influence of substrate bending is not taken into account. To validate the assumption of substrate bending, a 2D FEM model is used to model the active layer/thin-film/substrate bending due to the different contributions of the stress/strain components (Figure S3a, Supporting Information). Figure S3b, Supporting Information, shows the stress distribution within the thin film layer and the PET substrate at  $F = 10 \text{ N}$ . It can be clearly concluded that the highest stress occurs close to the stamp edge, which results in strong deformation. In this region, the deformation of the substrate induces a large longitudinal tensile strain component and a transverse compressive strain component within the thin film/active layer as shown in Figure S3c,S3d, Supporting Information. The results of the 2D FEM model clearly show that the experimentally measured piezoelectric response is strongly influenced by the transverse piezoelectric effect due to the bending of the flexible substrate and thus the active layer. The 3D polarization distribution spatial map shown in Figure 3e,f, obtained for  $F = 10 \text{ N}$  applied as force per unit area through a

boundary load condition, indicates that the maximum charge is generated at the edges of the nanostructure for both ZnO orientations, and decays substantially along the lateral dimensions.

This is important for obtaining site-specific pressure sensing with high lateral resolution and it is the advantage of using the nanostructuring approach. Contrarily, if the generated piezoelectric charge would be constant along the whole ZnO layer, the resolution of force sensing would be lower: the force response would be higher at the excitation location, where the force is applied, and would gradually decrease in the lateral direction.

## 2.2. Localized-Area Force Response

In order to demonstrate such site-specific sensing, a set of sensors is fabricated with a structured TE depicted in Figure 4a. The design relies on six electrode fields/pixels, each with an active area of  $0.5 \text{ mm} \times 0.5 \text{ mm}$  and 5 mm spacing between neighboring fields. In the experiment, pixel B1 was excited with a step force signal of 10 N applied through a stamp with  $d = 1 \text{ mm}$ , using the same piezoelectric test setup schematized in Figure S2a, Supporting Information. Minimum cross-talk between electrode fields/pixels is observed as shown in Figure 4b. Figure 4c shows the piezoelectric current time response of pixel B1 when excited over 4 cycles. A peak current  $I$  of 0.6 nA was measured, which translates to a piezoelectric charge  $Q = 170 \text{ pC}$  per step. Figure S4, Supporting Information, shows the generated charge from different pixels for step force excitations with magnitudes of 10 and 4 N. At  $F = 10 \text{ N}$ , a maximum charge  $Q = 270 \text{ pC}$  is measured for pixel A1 and a minimum charge  $Q = 100 \text{ pC}$  is measured for pixels B2 and C1, while for  $F = 4 \text{ N}$  a maximum charge of 170 pC and a minimum charge of 30 pC were measured for pixels A1 and C1, respectively. Variations in the measured charge at different pixels are attributed to thickness variations along the PUA imprint layer as explained in the SI. The sensor response to 5 cycles of force excitations from a finger touch is tested using the experimental setup schematized in Figure S2b, Supporting Information, where  $Q$  is calculated, showing a response of 216 to 252 pC with a signal rise time  $t_r = 0.75 \text{ s}$  (Figure 4d).

## 2.3. Humidity and Temperature Response

The sensor response upon humidity and temperature changes is measured in terms of piezoelectric charge in an environmental chamber as depicted in Figure S2c, Supporting Information. The response is measured from 25% up to 96% RH, using a sensor with a TE area of  $1 \text{ cm}^2$ . The charge response overtime at 25 °C for varying humidity conditions is shown in Figure 5a, while Figure 5b depicts the charge as a function of relative humidity. At 25 °C, the hydrogel is below its LCST ( $34 \pm 2 \text{ °C}$ ) and as a result has a high tendency to absorb water molecules, compared to the hydrogel at 40 °C, resulting in a maximum response of  $14.2 \pm 1 \text{ nC}$  at 96% RH. This is due to the polymer chain configuration, where strong hydrogen bonds between the hydrogel's hydrophilic functional groups (carboxylic and cyclic amide) and water molecules are present (Figure 5c,d).<sup>[54]</sup> The

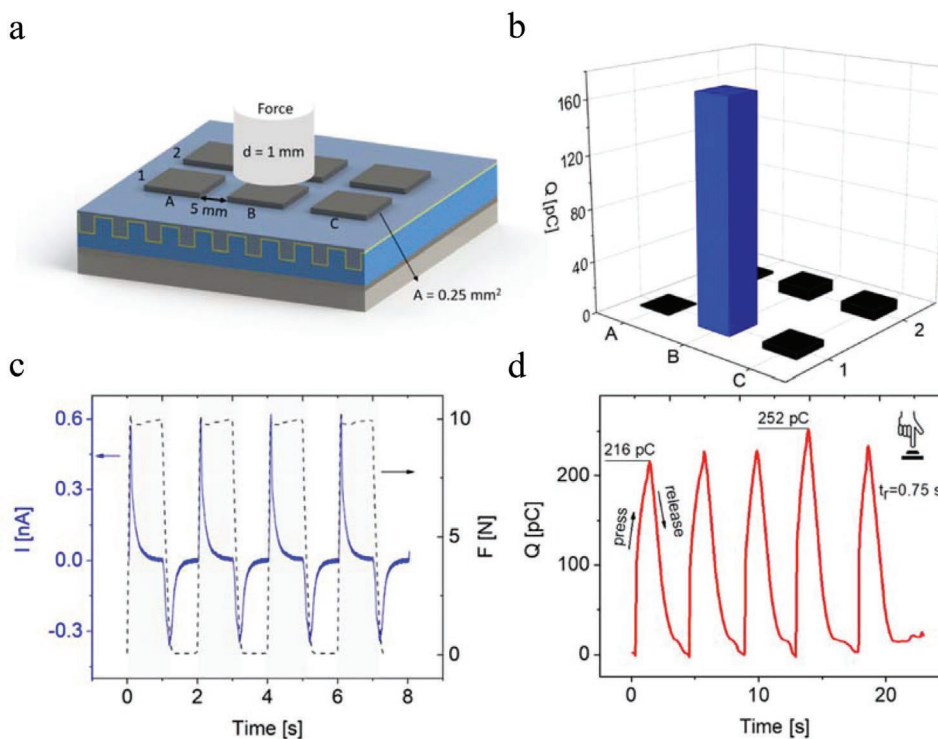


**Figure 4.** a) Schematics of six TE fields ( $A = 0.25\text{ mm}^2$ ) for localized response to force, where pixel B1 is excited with  $F = 10\text{ N}$ , using a force stamp with diameter  $d = 1\text{ mm}$  (dimensions are not shown to scale). b) 3D plot of piezoelectric charge response of pixel B1 and its neighboring pixels when excited with  $F = 10\text{ N}$ . c) Current  $I$  response of B1 over time,  $t$ , to  $10\text{ N}$  step force signal for 4 cycles. d) Sensor response to 5 cycles of force excitations from a finger touch with a maximum response  $Q = 252\text{ pC}$ .

sensor sensitivity,  $S_{H1}$ , at  $25\text{ }^\circ\text{C}$  is calculated to be  $0.1\text{ nC \%}^{-1}$  for the (relative) humidity range of 25 to 85% and  $S_{H2} = 1.2\text{ nC \%}^{-1}$  for the RH range between 85 and 96%. The previously observed non-linear increase in swelling<sup>[55]</sup> results in a high increase in  $S_{H2}$  above 85% RH. Figure 5b shows  $Q$  as a function of RH at 25 (below LCST) and  $40\text{ }^\circ\text{C}$  (above LCST) for the sensor with a hydrogel layer compared to a reference sensor. Above the LCST, a change in the hydrogel's polymer chain configuration occurs, which enhances inter- and intramolecular interactions between the hydrogel's hydrophobic groups resulting in less water absorption and incorporation into the hydrogel's mesh (coil-globule transition as depicted in Figure 5c).<sup>[54]</sup> The hydrogel experiences less swelling and thus lower stress is exerted onto the ZnO shell compared to that measured at  $25\text{ }^\circ\text{C}$ . Accordingly, above the LCST, the maximum response at 96% RH is  $4.0 \pm 0.3\text{ nC}$ , about one-third of the value at room temperature. At  $40\text{ }^\circ\text{C}$ , the sensitivity  $S_{H3}$  is calculated to be  $0.01\text{ nC \%}^{-1}$  between 25 and 85% RH and  $S_{H4} = 0.1\text{ nC \%}^{-1}$  between 85 and 96% RH. The reference sensor shows no response to humidity, confirming that the sensor response is indeed due to the hydrogel core swelling.

These observations with regard to humidity sensing are also confirmed by FEM simulations, which according to Figure 5e,f shows a maximum stress  $\sigma$  of  $174\text{ MPa}$  at 60% RH below the LCST versus  $13.4\text{ MPa}$  above LCST. The simulated charge response obtained from the FEM model (Figure 5b, dashed lines) is in very good agreement with the experimental data for both temperature conditions up to an RH of 80%. In addition,

in both cases, the maximum stress exerted on ZnO occurs at the edge of the nanostructures.

In the same experimental setup, the sensor response to temperature was investigated. Figure 6a displays the sensor response to a temperature profile at 96% RH. The temperature is gradually decreased from  $50$  to  $10\text{ }^\circ\text{C}$ , therefore ensuring that the hydrogel transitions from a low to high swelling regime (LCST =  $34 \pm 2\text{ }^\circ\text{C}$ ). The experiment was repeated for two different humidity levels (96% and 40%) as well as for the reference sensor and the corresponding charge curves are plotted as a function of temperature in Figure 6b. At 96% RH, the sensor temperature sensitivity,  $S_T$ , was found to be  $-0.14\text{ nC }^\circ\text{C}^{-1}$  within a temperature range between  $50$  ( $Q = 0.03\text{ nC}$ ) and  $30\text{ }^\circ\text{C}$  ( $Q = 2.1\text{ nC}$ ). Below  $30\text{ }^\circ\text{C}$ , a signal is measured but it does not change with temperature. This is a direct consequence of the hydrogel swelling profile, where the thickness changes around the LCST and stays constant for lower temperatures. However, no response to temperature was observed at low RH (40%), indicating that the hydrogel's sensitivity to temperature occurs around the LCST and at high RH.<sup>[55]</sup> This trend is also confirmed by FEM simulations, which indicate a saturation of the generated charge generation below  $30\text{ }^\circ\text{C}$  at 95% and 70% RH. Similar to the above-mentioned humidity characterization measurements, a reference sensor without a hydrogel layer measured at 96% RH in the temperature range of  $50$  to  $10\text{ }^\circ\text{C}$  and it showed no significant response to temperature.

Finally, yet importantly, we could use the sensor to detect the air blows from a human mouth from an approximate distance of

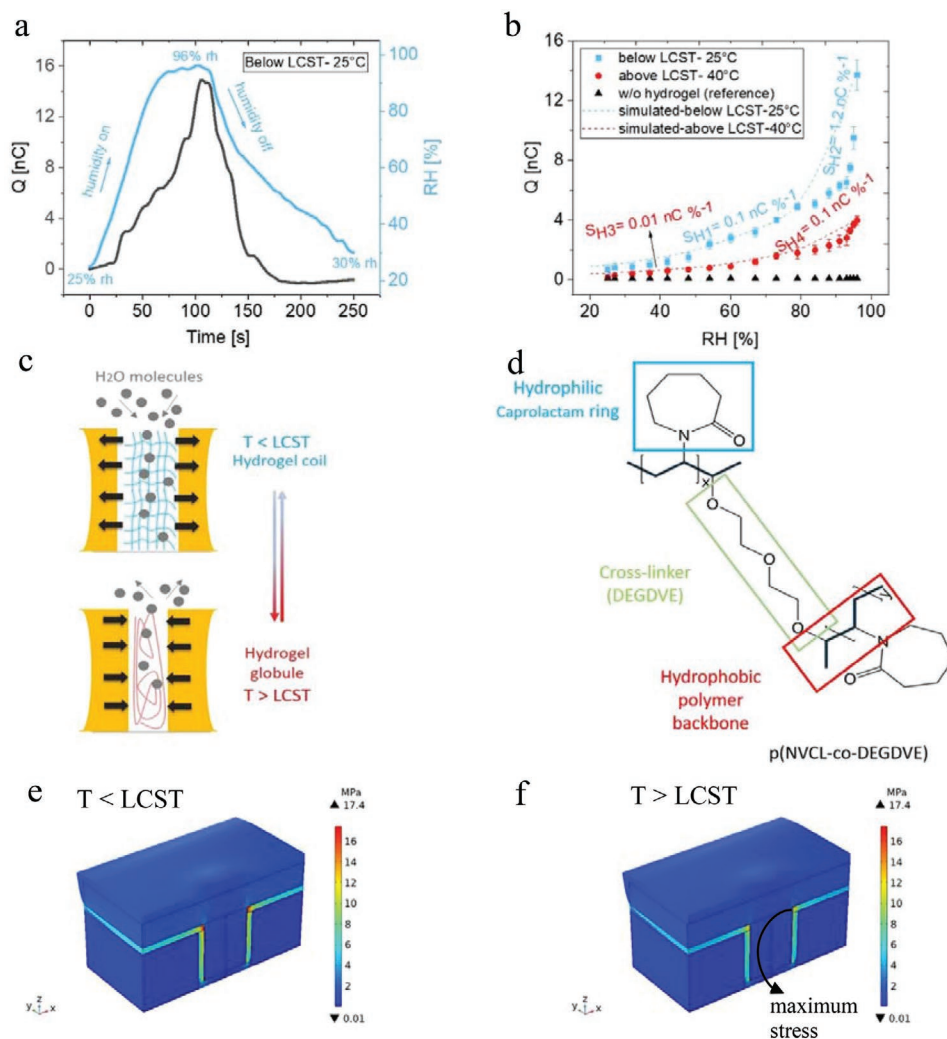


**Figure 5.** a) Sensor charge response to changes in humidity (RH = 25%–96%–30%) as a function of time. b) Humidity response of the sensor at 25 °C (below LCST) and 40 °C (above LCST), respectively, and a reference sensor (without a hydrogel), where  $S_{H_i}$  is indicated for four regions. The experimental data are averaged over 2 measurements ( $n = 2$ ) and the standard deviations are shown as error bars. Where the error bar is not visible, it is hidden by the data symbol. c) Schematics of hydrogel swelling mechanism and LCST influence on hydrogel swelling. d) Molecular structure of the hydrogel core. Stress distribution in the ZnO shell due to hydrogel swelling e) below and f) above LCST, obtained from FEM model.

10 cm using the experimental setup schematized in Figure S3b, Supporting Information. For the consecutive blows, the charge peaked with values between 0.65 to 0.78 nC (Figure 6c) and the signal rise time was about  $t_r = 1.1$  s (Figure 6d). The sensor response is attributed to highly humid air blown from the human mouth rather than to the induced temperature change as such an air blow has a relatively low temperature (30 °C).

### 3. Conclusion

In conclusion, we have demonstrated a multi-stimuli force, humidity, and temperature (F-H-T) responsive sensor fabricated on a flexible PET substrate for electronic skin applications. The sensor relies on combining piezoelectric ZnO with p(NVCL-co-DEGDVE) hydrogel into novel core-shell nanostructures. In a previous paper from our group, we demonstrated that the transition temperature of p(NVCL-co-DEGDVE) can

be tuned in a large range from ca. 40 to 15 °C.<sup>[33]</sup> This allows to tune its response to the desired temperature range. In this design, the used deposition conditions were chosen to obtain a transition at near-body temperature, which may be useful for artificial skin applications.

The core-shell nanorods are embedded into a nanopatterned PUA template. The sensor response to force is successfully demonstrated with an in-house piezoelectric measurement setup at different force magnitudes, applied parallel to the sensor's z-axis. The force-sensitivity is as high as  $S_F = 22\text{--}26$  pC N<sup>-1</sup>. As for the response to humidity and temperature, measurements in an environmental chamber revealed a maximum sensitivity to relative humidity of  $S_{H_2} = 1.2$  nC %<sup>-1</sup>, obtainable below the LCST of the hydrogel and at high relative humidity ( $\geq 85\%$  RH). Additionally, above the hydrogel LCST and at saturated relative humidity levels still, a sensitivity of  $S_{H_4} = 0.1$  nC %<sup>-1</sup> could be achieved, while a maximum sensitivity to temperature  $S_T = -0.14$  at 96% RH

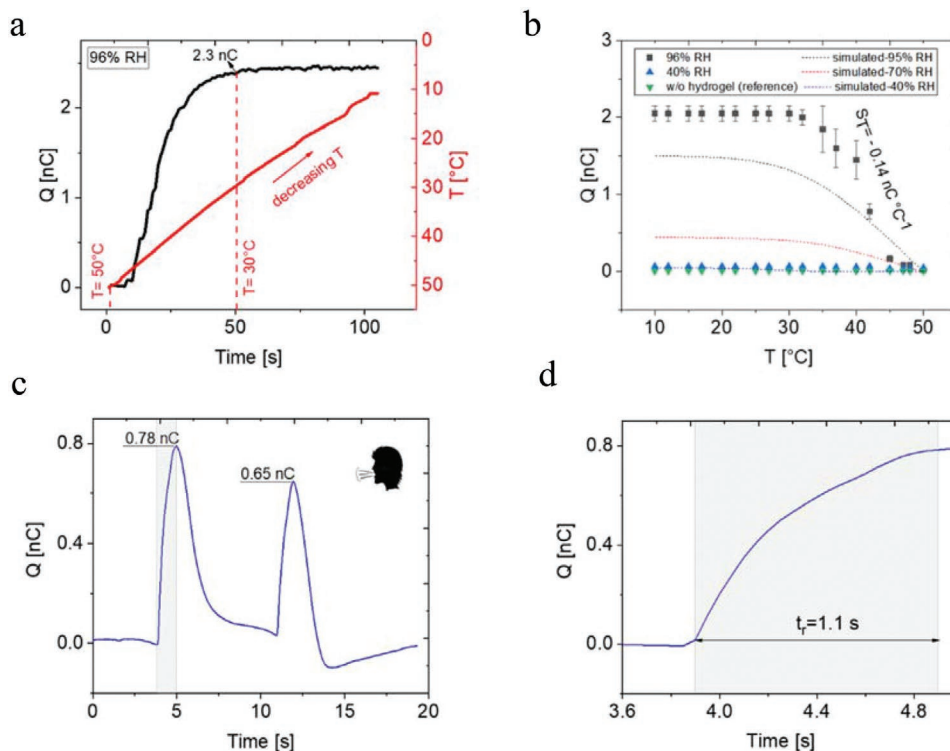


**Figure 6.** a) Sensor response  $Q$  to temperature  $T$  (50–10 °C) at 96% RH as a function of time. b)  $Q$  as a function of temperature at RH= 96% and 40% and a reference sensor without a hydrogel layer, with  $S_T$  indicated at 96% RH. The experimental data are averaged over 2 measurements ( $n = 2$ ) and the standard deviations are shown as error bars. Where the error bar is not visible, it is hidden by the data symbol. c) Sensor response to air blown from a human mouth, with a maximum  $Q = 0.78$  nC. d) zoomed-in Figure 6c showing signal rise time  $t_r = 1.1$  s.

is obtainable for a temperature range between 30 and 50 °C. The enhanced sensor sensitivity to humidity and temperature (in comparison to force) is a result of the nanostructuring approach,<sup>[14,56]</sup> which increases the contact surface area between the hydrogel core and the piezoelectric shell. We believe this difference in sensitivity for the different stimuli can be used for stimuli recognition, mainly by signal analysis. Alternatively, force and temperature can be distinguishable by slightly modifying the template/electrode design, to achieve pixels with nanorods filled with hydrogels and pixels filled only by ZnO.

The maximum force that was exerted on these sensors was 20N and sensor response was constant over the tested number of cycles. More detailed resilience and long-term stability tests are currently under investigation. In this design, temperatures in the range of 30–50 °C could be detected as shown in Figure 6b. Nevertheless, since the LCST of the p(NVCL-co-DEGDVE) can be tuned from 10 to 50 °C<sup>[33]</sup>, the window of temperature response can be expanded in future configurations.

Another advantage of this approach is that for force excitations parallel to the sensor's z-axis, the maximum charge is generated at the edges of the nanostructures and decays substantially along the lateral dimensions. This enables achieving site-specific force sensing with a very high spatial resolution, in principle, down to the dimensions of a single nanostructure, if the sensor electrodes were to be miniaturized to such dimensions. Using a design with adjacent square electrode fields each having only 0.25 mm<sup>2</sup>, a force excitation could be

spatially resolved with a negligible low cross-talk between neighboring fields. The sensor response times to force (28 ms), as well as humidity (25–50 s), are comparable to literature: reported response times to force are between 10 ms and 1 s, while to humidity the response time oscillates in the range 5–148 s.<sup>[14,16,18,19,30]</sup> Moreover, the sensor response is significantly faster than the system's intrinsic or excitation induced time scale and any delay comes from the specifics of excitation. Finally, the sensor response to a finger touch and air blown from a human mouth demonstrates the sensor applicability as e-skin element in real-life environment.

## 4. Experimental Section

**Fabrication:** The multi-stimuli  $F$ - $H$ - $T$  responsive sensor was fabricated according to the processing steps shown in Figure 1b. Starting with a 125  $\mu\text{m}$  thick polyethylene terephthalate (PET) substrate with dimensions of 90  $\times$  60 mm<sup>2</sup> (Melinex STS 505, Dupont Teijen Films), e-beam evaporation was used to deposit an ultra-thin (2.5 nm) chromium adhesion layer, followed by a layer of silver (50 nm) serving as a BE. An e-beam deposition rate between 0.10 and 0.25 nm s<sup>-1</sup> was applied. The BE had an active area of 75  $\times$  40 mm<sup>2</sup>. Then, a resin based on PUA (NILcure, Joanneum Research) was deposited manually using a glass pipette (resin volume  $\approx$  1 mL) and nanostructured by UV nanoimprint lithography (UV-NIL) using a UV light source (USDT-20ML-8R, Biostep) with a wavelength  $\lambda = 365$  nm and a curing time  $t_{\text{cur}}$  of 60 s. For imprinting, a transparent polymeric stamp (NILcure, Joanneum Research) was first prepared from a cyclic olefin copolymer master (COC, STRATEC Consumables GmbH and Fianostics GmbH)

following the same UV-NIL parameters/procedure described above. The nanostructures, that is, nanoholes, on the master had a diameter  $d = 500$  nm, height  $H = 500$  nm, aspect ratio  $AR = 1$ , and a pitch = 1000 nm and were arranged in 16 square fields each  $8 \times 8$  nm structured squares. During imprinting, a force  $F = 30$  N was maintained on the stamp for 30 min to reduce the imprint layer to the desired thickness  $t$ . Finally, after stamp demolding, a UV-post curing step (395 nm, 120 s) (BLD-240-C210-ERS, uPowerTek) was performed. To form the piezoelectric shell, a thin ZnO layer (50 nm) was deposited at 35 °C into the nanostructured PUA template by means of PEALD, with a custom-built direct plasma ALD reactor used. The reactor has an asymmetrical plate configuration, in which the radio frequency (RF) and the ground electrode were 18 and 20 cm in diameter, respectively. A distance of 11 cm was maintained between both electrodes. Diethyl zinc (DEZn, Dock/Chemicals) flow into the reactor was controlled by an ALD-valve (ALD3, Swagelok). An RF plasma power generator (Cesar 13.56 MHz, Advanced Energy) was used to deliver the required input power through a matching network (Navio, Advanced Energy). Oxygen ( $O_2$ ) and argon (Ar) were flown into the reactor using a mass flow controller (MFC-GE50A, MKS) with a flow rate set to 20 sccm.  $O_2$  was flown into the reactor during the plasma step, while Ar was used as a purging gas. The pump system in use consisted of a rotary vane pump (DUO 20, Pfeiffer Vacuum) and a turbomolecular pump (TMH071P, Pfeiffer Vacuum). Using a butterfly valve (MKS 253B), the pressure was set to 200  $\mu$ bar during the plasma step. At 35 °C, 250 cycles were needed to deposit 50 nm of ZnO. A single cycle consists of 1) an  $O_2$  plasma step, 2) an Ar purging step, 3) a DEZ step, and 4) an Ar purging step.

Subsequently, the p(NVCL-co-DEGDVE) hydrogel core was deposited using iCVD in an in-house built reactor. Deposition of 200 nm p(NVCL-co-DEGDVE) was carried out by in-flowing NVCL (98% stabilized, Sigma Aldrich) at a constant flow rate of 0.275 sccm, DEGDVE cross-linker (99%, Sigma Aldrich) at a flow rate of 0.25 sccm, and tert-butyl peroxide (TBPO) initiator (98%, Sigma Aldrich) at a flow rate of 2 sccm into the reactor. The filament temperature was set to 200 °C and the stage/substrate temperature to 35 °C. More details on the reactor can be found elsewhere.<sup>[57]</sup>

As a last fabrication step, the TE was formed by depositing a 50 nm Ag layer on top using e-beam evaporation. The TE has an active area of 1 cm<sup>2</sup> for one set of samples. Another set of samples was fabricated with six neighboring TE fields/pixels (electrode active area of 0.25 mm<sup>2</sup>) spaced 5 mm apart. This design was utilized to test the sensor response to localized force excitations as well as the cross-talk between neighboring TE fields/pixels.

**Characterization:** Images of the imprint stamp, template layer, nanostructures, ZnO shell, and p(NVCL-co-DEGDVE) hydrogel core were obtained with a scanning electron microscope (SEM, part of an e-line system, RAITH GmbH). Cuts for cross-sectional SEM imaging were performed using an ultra-knife (MC 13858, DiATOME) with a knife angle of 45° and cut speed of 1 mm s<sup>-1</sup>. The sensor dielectric properties were measured using an LCR meter (Hioki 3532–50 LCR HiTESTER, Hioki E.E Corporation), in a frequency range of  $f = 42$  Hz to 5 MHz. I-V measurements were performed in the voltage range  $V = \pm 20$  V using a parameter analyzer (PA1004, MB technology). Sensor response measurements to external force were carried out using an in-house built setup at  $F = 4, 10, 12, 15,$  and 20 N. More details on the setup can be found elsewhere.<sup>[36]</sup> Sensor response measurements to humidity were performed in a commercial environmental chamber (SH-222, ESPEC) at relative humidity  $RH = 25$ –96% and temperature  $T = 25$  and 40 °C. Due to condensation inside the humidity chamber, a relative humidity below 25% was not obtainable. The generated current was converted into a voltage signal using a transimpedance amplifier (TIA) and recorded with a data acquisition system (SIRIUS Multi, Dewesoft). The charge  $Q$  was then calculated from the calibrated V-I signal via numerical integration. The sensor response to temperature was measured using the same setup as used for humidity measurements with a temperature range of  $T = 50$ –10 °C, at  $RH = 40$  and 96%. Finally, the sensor response to real-life stimuli, namely excitation by finger touch and air blown from a human mouth was measured using the Dewesoft data acquisition

system, similarly to humidity and temperature response measurements. The data were displayed as mean values with standard deviations. The sample size  $n$  was indicated in each figure, where applicable.

**FEM Simulations:** COMSOL Multiphysics V5.6 in combination with the Structural Mechanics module was used to model the sensor response to external stimuli, namely, force, humidity, and temperature. A multiphysics coupling was applied to account for the piezoelectric effect. A 3D geometry model of only half a single nanorod was used and proper symmetry boundary conditions were applied on the  $xz$ -plane of the geometry. Additionally, a periodic boundary condition was applied on the  $yz$ -plane to obtain the response over a periodic number of nanorods. The top and BEs were represented by floating potential and ground boundary conditions, respectively. The hydrogel swelling behavior was modeled following Equation (1) using the hygroscopic swelling node in COMSOL Multiphysics. Laser interferometry was used to obtain the thickness change due to swelling and dependently the data shown in Table S1, Supporting Information. The PUA template was modeled as a linear elastic material and the ZnO shell as piezoelectric material (piezoelectric coupling matrix imported from COMSOL material library,  $d_{33} = 11.7$  pC N<sup>-1</sup>). Force excitations were applied as force per unit area using a boundary load condition.

Additionally, substrate/active layer bending due to applied force in the piezoelectric characterization setup was investigated using a simplified 2D model identical to the experimental setup. It consisted of a hard flat stamp with radius  $r = 2.5$  mm getting in contact with and deforming a layer stack comprising the sensor element. In this model, the sensor (active layer) consisted of a flat unstructured anisotropic thin film layer with a thickness of 6  $\mu$ m, poisson's ratio  $\nu$  of the active layer was assumed isotropic (Table S2, Supporting Information), on top of a PET substrate with a thickness of 125  $\mu$ m and a sample support out of rubber with thickness 5 mm, as depicted in Figure S3a, Supporting Information. A symmetry line existed at  $x = 0$  mm. All materials were assumed to behave linearly elastic, except for the active layer, for which material's effective elastic properties were first derived from a representative volume element (RVE) based on a unit cell containing a single nanorod. The contact boundary condition was applied to the bottom boundary of the stamp (source) and the top boundary of the thin film/active layer (drain), while the top side of the stamp was successively displaced to obtain a total stamp force  $F = 0$ –20 N.

## Supporting Information

Supporting Information is available from the Wiley Online Library or from the author.

## Acknowledgements

This project has received funding from the European Research Council (ERC) under the European Union's Horizon 2020 research and innovation program (Grant Agreement No. 715403). The authors thank STRATEC Consumables GmbH and Fianostics GmbH for providing the COC master. In addition, the authors acknowledge Marlene Anzengruber for the hydrogel swelling measurements.

## Conflict of Interest

The authors declare no conflict of interest.

## Data Availability Statement

The data that support the findings of this study are available from the corresponding author upon reasonable request.

## Keywords

electronic skins, humidity sensors, hydrogels, multi-stimuli responsive sensors, nanofabrication, piezoelectric zinc oxide, pressure sensors, temperature sensors

Received: February 15, 2022

Revised: March 31, 2022

Published online: May 11, 2022

- [1] D. De Rossi, F. Carpi, E. P. Scilingo, *Adv. Colloid Interface Sci.* **2005**, 116, 165.
- [2] W. L. Jenkins, *Methods of psychology*, John Wiley & Sons Inc, Hoboken, NJ, US **1948**, pp. 250–267.
- [3] M. Denda, M. Nakatani, K. Ikeyama, M. Tsutsumi, S. Denda, *Exp. Dermatol.* **2007**, 16, 157.
- [4] D. Filingeri, G. Havenith, *Temperature* **2015**, 2, 86.
- [5] M. L. Hammock, A. Chortos, B. C. K. Tee, J. B. H. Tok, Z. Bao, *Adv. Mater.* **2013**, 25, 5997.
- [6] X. Wang, L. Dong, H. Zhang, R. Yu, C. Pan, Z. L. Wang, *Adv. Sci.* **2015**, 2, 1500169.
- [7] J. C. Yang, J. Mun, S. Y. Kwon, S. Park, Z. Bao, S. Park, *Adv. Mater.* **2019**, 31, 1904765.
- [8] Z. Ma, S. Li, H. Wang, W. Cheng, Y. Li, L. Pan, Y. Shi, *J. Mater. Chem. B* **2019**, 7, 173.
- [9] N. Yogeswaran, W. Dang, W. T. Navaraj, D. Shakhthivel, S. Khan, E. O. Polat, S. Gupta, H. Heidari, M. Kaboli, L. Lorenzelli, G. Cheng, R. Dahiya, *Adv. Robot.* **2015**, 29, 1359.
- [10] W. Chen, X. Yan, *J. Mater. Sci. Technol.* **2020**, 43, 175.
- [11] M. Xie, K. Hisano, M. Zhu, T. Toyoshi, M. Pan, S. Okada, O. Tsutsumi, S. Kawamura, C. Bowen, *Adv. Mater. Technol.* **2019**, 4, 1800626.
- [12] Z. Li, M. Zhu, J. Shen, Q. Qiu, J. Yu, B. Ding, *Adv. Funct. Mater.* **2020**, 30, 1908411.
- [13] Q. Li, L. Chen, M. Guo, Z. Hu, *Adv. Mater. Technol.* **2021**, 2101371, <https://doi.org/10.1002/admt.202101371>.
- [14] G. Schwartz, B. C. K. Tee, J. Mei, A. L. Appleton, D. H. Kim, H. Wang, Z. Bao, *Nat. Commun.* **2013**, 4, 1859.
- [15] B. C. K. Tee, C. Wang, R. Allen, Z. Bao, *Nat. Nanotechnol.* **2012**, 7, 825.
- [16] J. W. Park, J. Jang, *Carbon N. Y.* **2015**, 87, 275.
- [17] T. Q. Trung, L. T. Duy, S. Ramasundaram, N. E. Lee, *Nano Res.* **2017**, 10, 2021.
- [18] W. Jeong, J. Song, J. Bae, K. R. Nandanapalli, S. Lee, *ACS Appl. Mater. Interfaces* **2019**, 11, 44758.
- [19] H. Guo, C. Lan, Z. Zhou, P. Sun, D. Wei, C. Li, *Nanoscale* **2017**, 9, 6246.
- [20] J. H. Oh, S. Y. Hong, H. Park, S. W. Jin, Y. R. Jeong, S. Y. Oh, J. Yun, H. Lee, J. W. Kim, J. S. Ha, *ACS Appl. Mater. Interfaces* **2018**, 10, 7263.
- [21] Z. Cao, Y. Yang, Y. Zheng, W. Wu, F. Xu, R. Wang, J. Sun, *J. Mater. Chem. A* **2019**, 7, 25314.
- [22] G. Liu, Q. Tan, H. Kou, L. Zhang, J. Wang, W. Lv, H. Dong, J. Xiong, *Sensors* **2018**, 18, 1400.
- [23] Y. Chen, B. Lu, Y. Chen, X. Feng, *Sci. Rep.* **2015**, 5, 11505.
- [24] M. Khatib, O. Zohar, W. Saliba, H. Haick, *Adv. Mater.* **2020**, 32, 2000246.
- [25] H. Liu, H. Xiang, Y. Wang, Z. Li, L. Qian, P. Li, Y. Ma, H. Zhou, W. Huang, *ACS Appl. Mater. Interfaces* **2019**, 11, 40613.
- [26] J. Kim, M. Lee, H. J. Shim, R. Ghaffari, H. R. Cho, D. Son, Y. H. Jung, M. Soh, C. Choi, S. Jung, K. Chu, D. Jeon, S. T. Lee, J. H. Kim, S. H. Choi, T. Hyeon, D. H. Kim, *Nat. Commun.* **2014**, 5, 5747.
- [27] L. Wang, J. A. Jackman, E. L. Tan, J. H. Park, M. G. Potroz, E. T. Hwang, N. J. Cho, *Nano Energy* **2017**, 36, 38.
- [28] X. Zhao, Y. Long, T. Yang, J. Li, H. Zhu, *ACS Appl. Mater. Interfaces* **2017**, 9, 30171.
- [29] L. Zhu, Y. Wang, D. Mei, W. Ding, C. Jiang, Y. Lu, *ACS Appl. Mater. Interfaces* **2020**, 12, 31725.
- [30] D. H. Ho, Q. Sun, S. Y. Kim, J. T. Han, D. H. Kim, J. H. Cho, *Adv. Mater.* **2016**, 28, 2601.
- [31] S. Han, N. U. H. Alvi, L. Granl f, H. Granberg, M. Berggren, S. Fabiano, X. Crispin, *Adv. Sci.* **2019**, 6, 1802128.
- [32] B. Lee, A. Jiao, S. Yu, J. B. You, D. H. Kim, S. G. Im, *Acta Biomater.* **2013**, 9, 7691.
- [33] F. Muralter, A. Perrotta, O. Werzer, A. M. Coclite, *Macromolecules* **2019**, 52, 6817.
- [34] L. Yicheng, N. W. Emanetoglu, Y. Chen, *Zinc Oxide Bulk, Thin Films and Nanostructures*, Elsevier Science Ltd, Oxford, UK **2006**, pp. 443–489.
- [35] D. Bremecker, P. Keil, M. Gehringer, D. Isaia, J. R del, T. Fr mling, *J. Appl. Phys.* **2020**, 127, 034101.
- [36] T. Abu Ali, J. Pilz, P. Sch ffner, M. Kratzer, C. Teichert, B. Stadlober, A. M. Coclite, *Phys. Status Solidi A* **2020**, 217, 2000319.
- [37] J. Rao, Z. Chen, D. Zhao, R. Ma, W. Yi, C. Zhang, D. Liu, X. Chen, Y. Yang, X. Wang, J. Wang, Y. Yin, X. Wang, G. Yang, F. Yi, *Nano Energy* **2020**, 75, 105073.
- [38] G. Ozaydin-Ince, K. K. Gleason, *Chem. Vap. Deposition* **2010**, 16, 100.
- [39] K. Tapily, D. Stegall, D. Gu, H. Baumgart, G. Namkoong, A. Elmustafa, *ECS Trans.* **2009**, 25, 85.
- [40] H. Kim, U. S. Jung, S. I. Kim, D. Yoon, H. Cheong, C. W. Lee, S. W. Lee, *Curr. Appl. Phys.* **2014**, 14, 166.
- [41] C. Zhimin, L. Xinchun, H. Dannong, *Surf. Coat. Technol.* **2012**, 207, 361.
- [42] C. Y. Yen, S. R. Jian, G. J. Chen, C. M. Lin, H. Y. Lee, W. C. Ke, Y. Y. Liao, P. F. Yang, C. T. Wang, Y. S. Lai, J. S. C. Jang, J. Y. Juang, *Appl. Surf. Sci.* **2011**, 257, 7900.
- [43] K. Tapily, D. Gu, H. Baumgart, G. Namkoong, D. Stegall, A. A. Elmustafa, *Semicond. Sci. Technol.* **2011**, 26, 115005.
- [44] L. Zhu, *J. Phys. Chem. Lett.* **2014**, 5, 3677.
- [45] M. F llbrandt, E. Ermilova, A. Asadujjaman, R. H lzel, F. F. Bier, R. von Klitzing, A. Sch nhals, *J. Phys. Chem. B* **2014**, 118, 3750.
- [46] F. Biryani, A. M. Abubakar, K. Demirelli, *Thermochim. Acta* **2018**, 669, 66.
- [47] J. Pilz, A. Perrotta, P. Christian, M. Tazreiter, R. Resel, G. Leising, T. Griesser, A. M. Coclite, *J. Vac. Sci. Technol., A* **2018**, 36, 01A109.
- [48] J. Pilz, A. Perrotta, G. Leising, A. M. Coclite, *Phys. Status Solidi* **2020**, 217, 1900256.
- [49] M. Laurenti, S. Stassi, M. Lorenzoni, M. Fontana, G. Canavese, V. Cauda, C. F. Pirri, *Nanotechnology* **2015**, 26, 215704.
- [50] N. J. Blumenstein, F. Streb, S. Walheim, T. Schimmel, Z. Burghard, J. Bill, *Beilstein J. Nanotechnol.* **2017**, 8, 296.
- [51] S. J. Kang, Y. H. Joung, *Appl. Surf. Sci.* **2007**, 253, 7330.
- [52] X. Yan, W. Ren, H. Xin, P. Shi, X. Chen, X. Wu, *Ceram. Int.* **2013**, 39, S583.
- [53] G. J. T. Leighton, Z. Huang, *Smart Mater. Struct.* **2010**, 19, 065011.
- [54] S. Kozano glu, T.  zdemir, A. Usanmaz, *J. Macromol. Sci.* **2011**, 48, 467.
- [55] F. Muralter, F. Greco, A. M. Coclite, *ACS Appl. Polym. Mater.* **2020**, 2, 1160.
- [56] S. Park, H. Kim, M. Vosgueritchian, S. Cheon, H. Kim, J. H. Koo, T. R. Kim, S. Lee, G. Schwartz, H. Chang, Z. Bao, *Adv. Mater.* **2014**, 26, 7324.
- [57] F. Muralter, A. Perrotta, A. M. Coclite, *Macromolecules* **2018**, 51, 9692.
- [58] S. H. Ahn, L. J. Guo, *ACS Nano* **2009**, 3, 2304.